Biophysical Journal, Volume 99

**Supporting Material**

# DENDRITIC SIGNALS COMMAND FIRING DYNAMICS IN A MATHEMATICAL MODEL OF CEREBELLAR PURKINJE CELL

Stephane Genet, Loic Sabarly, Emmanuel Guigon, Hugues Berry, and Bruno Delord

# Supplementary Material

Dendritic signals command firing dynamics in a mathematical model of cerebellar Purkinje cell

Stéphane Genet, Loïc Sabarly, Emmanuel Guigon, Hugues Berry and Bruno Delord

## I. Models of membrane currents and internal Ca regulation

### Membrane ion currents involved in plateau/valley potentials and bistability

The abolishment of PC plateaus by Na and Ca channels blockers and the upward shifts of the plateau voltage following partial blockage of K conductances early suggested that the amplitude and time course of these signals result from a balance of hyperpolarizing K currents and depolarizing currents (Na in the soma and Ca in dendrites (4)). However, models incorporating a detailed description of PC currents proved unable to replicate these signals (38). At about the same time, Yuen et al. (15) attempted to extract from the wealth of active PC currents the minimal set of currents required to produce dendritic Ca-dependent spikes and plateaus. They demonstrated that the set of P-type Ca current, $I_{CaP}$, and delayed rectifier K current, $I_{Kdr}$, can produce both plateaus and spikes. This finding agreed with *(i)* the fact that ω-Aga-IVA, a selective antagonist of P/Q-type channels (39), abolishes both dendritic spikes and plateaus and (*ii*) the existence of high-threshold delayed rectifier K currents (40) serving to repolarize spikes (41). However, plateaus in this simplified model had unrealistically large amplitude (~60 mV) and a higher voltage threshold than spikes, whereas experiments evidence that Ca spikes ride on plateaus (2, 4). These discrepancies suggested a basic flaw in our knowledge of PC currents at the time when these models were built, most probably regarding K currents since P/Q channels had been shown to underlie ~90 % of total Ca currents in PC (5, 42-44).

Most notably, Etzion and Grossman (45, 46) subsequently identified a highly 4-aminopyridine sensitive delayed rectifier K current in PC and demonstrated that it underlies the sharp outward rectification in the *I-V* relationship of PC near the plateau level, which is visible after blocking inward currents (47). They also reported that partial blocking of this K current reduces latency to the onset of Ca spikes firing in responses to intracellular current pulses (46). Because Ca spikes ride on dendritic plateaus (4), these findings suggested a crucial participation of this K current to the electrogenesis of dendritic plateaus. We have shown that adding a crude description of this current, termed $I_{Ksub}$, to the Yuen et al.'s model (15) together with the modulation of P/Q-type Ca currents amplitude due to changes in the Nernst potential of $Ca^{2+}$ ions resulting from $Ca^{2+}$ elevations in the cytoplasm (24) results in a simple (three state variables) biophysical model producing plateaus and spikes with realistic thresholds and shapes (11). To our knowledge, it remains the sole biophysically-grounded model correctly reproducing the PC dendrites dual electroresponsiveness. This model predicts mirror signals to plateaus, termed valleys potentials, by which brief inhibitory synaptic inputs trigger long lasting hyperpolarizations of PC. The recent demonstration that most of voltage-dependent K channels in PC belong to the family of high-threshold Kv3 channels (32, 46, 48-50) strengthens the model's conclusion that the interplay between high threshold Ca and K channels constitutes the backbone of PC dendrites' dual electroresponsiveness. In particular, Bushell et al. (51) have demonstrated that high-threshold, Kv3-like voltage-dependent channels underlie the outward rectifying K current (the model's $I_{Ksub}$), as originally suspected by Etzion and Grossman (46). The recent study of Martina et al. (50), which demonstrates that

PC express exceptionally fast K currents legitimates the assumption of instantaneous activation of $I_{Ksub}$ in the model. Moreover, studies on other types of Ca currents identified in PC (L, T and R) give no indication that they are involved in dendritic plateaus.

**Intrinsic membrane currents**

In the model, the density of all currents $I$ (nA/cm$^2$) obeys Ohm's law, $I = g\left(V - E\right)$, in which $g$ (μS/cm$^2$) denotes the conductance density, $V$ (mV) the membrane potential and $E$ the Nernst equilibrium potential (mV). The conductance $g$ is determined by the product of a maximum conductance, $\bar{g}$ and a gating variable, $m$, representing the fraction of activated channels

$$g\left(V,\left[Ca\right]_i\right) = \bar{g}\, m\left(V,\left[Ca\right]_i\right)^p . \tag{SI1}$$

Variable $m$ is a function of $V$ (for voltage-dependent channels) and possibly of the internal Ca concentration, $[Ca]_i$ (for Ca-dependent potassium channels, see below). In the case of A-type K channels, equation (SI1) is multiplied by a second $m$-like variable modeling their inactivation properties.

Kinetics of the $m$ variable of all voltage dependent currents but $I_{Na}$ is modeled by a simplified version of the classical Hodgkin-Huxley (52) rate equation

$$\tau_m\left(V\right)\frac{\partial m}{\partial t}\left(V\right) = m_\infty\left(V\right) - m , \tag{SI2}$$

in which the steady-state value $m_\infty$ of $m$ depends on $V$ according to a Boltzmann function (see e.g., (53))

$$m_\infty\left(V\right) = 1/\left[1 + \exp\left(\pm(V - V_m)/k_m\right)\right] . \tag{SI3}$$

$V_m$ (mV) is the half-activation potential and $k_m$ (mV) the slope of change of $m_\infty$ with $V$. The '–' and '+' signs stand for activation and inactivation variables respectively.

P/Q-type Ca channels which are responsible for $I_{CaP}$ and Kv3 potassium channels like those underlying the outward rectification modeled by $I_{Ksub}$ activate very fast (42, 50, 54). As a simplifying hypothesis, our model accordingly assumes that $\tau_m = 0$ (i.e. instantaneous activation) and hence that $m = m_\infty$ at each time point for these currents (see Eq. SI2). By contrast, $I_{Kdr}$ has a larger voltage-dependent time constant of activation that is taken from (15)

$$\tau_m\left(V\right) = \tau_{m0} + \tau_{m1}/\left[\exp\left(\left(V + V_{\tau m}\right)/k_{\tau m}\right) + c_{\tau m}/\exp\left(\left(V + V_{\tau m}\right)/k_{\tau m}\right)\right] , \tag{SI4}$$

with $\tau_{m0}$ = 0.2 ms, $\tau_{m1}$ = 4.15 ms, $V_{\tau m}$ = –22.5 mV, $k_{\tau m}$ = 17 mV and $c_{\tau m}$ = 0.6.

Voltage-dependent sodium channels in the PC soma belong to the Nav1.6 type (54, 55). These channels deviate from the classical Hodgkin-Huxley formalism in that they produce resurgent currents upon repolarization which have been implicated in the high-frequency SS firing of PC (56). We model dynamics of the $m$ variable of $I_{Na}$ according to the kinetic scheme of Raman and Bean (56). The voltage dependence of rate constants $\alpha$, $\beta$ and $\zeta$ is shifted by +14 mV to produce SS with a voltage threshold consistent with latest data (17, 33).

We simulated variants of the basic dendritic model encompassing recently documented conductances to evaluate the robustness of its conclusions. Several studies

suggest that an important role of P/Q type Ca channels is to provide a source of $Ca^{2+}$ ions to activate KCa channels (57, 58). PC express both SK and BK-type KCa channels (57-63). BK channels behave much like delayed-rectifier K channels, with the difference that their $V_m$ decreases with increasing Ca levels (20). Our model of their currents uses the modified Boltzmann function for $m_\infty$ derived by Womack and Khodakhah (59) from their data on BK channels in PC, in which $k_m = RT/\bar{z}F$. We take $\bar{z}$ = 2.0366 (mean value computed from Table 1 in (59)) and $\tau_m$=1.8ms (59). The Ca-dependence of $V_m$ is modeled by the function

$$V_m = -45 + 362.8\exp\left(-\left[Ca\right]_i^{0.35}/0.96\right), \tag{SI5}$$

representing the best non-linear fit of data in Table 1 in (59).

Unlike the BK kind of KCa channels, $Ca^{2+}$ ions directly activate SK channels. A precise characterization of SK channels in PC is lacking but experiments have consistently reported a fast and non-linear activation of these channels in numerous cell types (64). In the absence of conflicting results, we accordingly assume instantaneous $Ca^{2+}$ activation of PC SK channels, using a simple Hill equation for their $m_\infty$ variable

$$m_\infty = \frac{\left[Ca\right]_i^z}{{K_{SK}}^z + \left[Ca\right]_i^z} \tag{SI6}$$

A mean $z$ = 5 value is adopted from the comprehensive review of Xia et al. (64) on SK channels. $K_{SK}$ is taken as 300 nM (affinity constant of cloned SK2 channels (65), the SK channel subtype found in PC (60)).

The hyperpolarization-activated cationic current $I_h$ (66), which is segregated to dendrites where it exhibits a uniform density (67), has been implicated in bistable properties of PC (7, 8). Our simulations of $I_h$ uses the experimentally-constrained model of this current given by Khaliq et al. (68).

We derived a model of A-type K currents active at sub-threshold potentials from data of Sacco and Sampia (69). Voltage-dependence for the time constant of their *m* activation variable was fitted to data from these authors with equation $\tau_m = t_0 + t_1/\left[\exp\left(\left(V - V_\tau\right)/k_\tau\right) + c_t/\exp\left(\left(V - V_\tau\right)/k_\tau\right)\right]$, in which parameters were $t_0 = 1.055$ and $t_1 = 5.25$ (ms), $k_\tau = 15.7$ mV, $V_\tau = -59.28$ mV and $c_t = 0.785$ (dimensionless). A mean 950 ms value is adopted for their weakly voltage-dependent time constant of inactivation.

With the exception of the well-established segregation of Na channels to the soma and Ca channels to dendrites, our model assumes that all other channels are uniformly smeared over the somato-dendritic membrane of PC. The Nernst potential of the leakage, Na and K currents are constants while that of $I_{CaP}$ depends on the variable $[Ca]_i$ according to the Nernst formula, $E_{Ca} = \frac{RT}{2F}\ln\frac{\left[Ca\right]_o}{\left[Ca\right]_i}$, in which $[Ca]_o$ denotes the (fixed) external $Ca^{2+}$ ion concentration. To obtain the $Ca^{2+}$ PDE of the model, we added a longitudinal diffusion term to the balance equation of $Ca^{2+}$ ions (Eq. 12 in (11)). From Fick's law, this diffusion flux across a dendrite section reads $-D_{Ca}\pi\delta\left(2R_d - \delta\right)\frac{\partial\left[Ca\right]_i}{\partial x}$ (mol/s), with $D_{Ca}$ ($cm^2/s$) denoting the diffusion coefficient and $\delta$ (cm) the thickness of the cytoplasm layer where free $Ca^{2+}$ ions are confined (see (11)). Table 1 lists the standard values of ion current parameters whereas Table 2 provides values of geometric, electric and internal Ca regulation parameters.

# TABLES

| | Current name | Abbrev | $E$ (mV) | $p$ | $V_m$ (mV) | $k_m$ (mV) | $\overline{g}$ (μS/cm$^2$) |
|---|---|---|---|---|---|---|---|
| Ion currents in the basic G&D model | P-type Ca | $I_{CaP}$ | *Eq*. 7 | 1 | -22 | 4.53 | 600 (d)<br>0 (s) |
| | delayed-rectifier K | $I_{Kdr}$ | -95 | 4 | -25 | 11.5 | 4200 (s)<br>24500 (d) |
| | sub-threshold K | $I_{Ksub}$ | -95 | 3 | -44.5 | 3 | 30 |
| | leakage | $I_{Leak}$ | -60 | | passive | | 20 |
| Other PC ion currents introduced in variant models | Na | $I_{Na}$ | 60 | | model of Raman and Bean (56) | | 25000 (s)<br>0 (d) |
| | BK calcium activated K | $I_{KCaBK}$ | -95 | | Eq. 5 and 6 | | adjustable |
| | SK calcium activated K | $I_{KCaSK}$ | -95 | | Eq. 7 | | adjustable |
| | hyperpolarization activated cationic | $I_h$ | -30 | | model of Khaliq et al. (68) | | adjustable |
| | sub-threshold A-type K | $I_A$ | -85 | Activation<br>1 | -24.9 16.2 | Inactivation<br>1 | -69.2 9.7 | adjustable |

**Table 1. Parameters of membrane currents. Abbreviations: (s): soma, (d): dendrites**

| | Parameter | Description | Value | Notes |
|---|---|---|---|---|
| Geometric | $R_d$ | radii of spiny dendrites | 2 μm (primary segments)<br>1.4 μm (secondary)<br>1 μm (tertiary) | (19) |
| | $\delta$ | thickness of cytoplasmic shell in dendrites | $3 \times 10^{-5}$ cm | (11) |
| | | | | |
| | $q$ | ratio of somatic to total cell surfaces | $5 \times 10^{-2}$ | (19) |
| | $N_s$ | linear spine density | 21 $\mu m^{-1}$ (spiny dendrites)<br>2 $\mu m^{-1}$ (smooth dendrites) | (70) |
| | | | | |
| Ca dynamics | $k$ | one-dimensional Ca diffusion constant | 0.01 cm/s | (11) |
| | $[B]_T$ | Ca buffer concentration | 150 μM | (11) |
| | $K_d$ | dissociation constant of buffer | 1 μM | (11) |
| | $[Ca]_b$ | cytoplasmic basal free Ca concentration | 50 nM | (11) |
| | $[Ca]_o$ | external free Ca concentration | 1.1 mM | (11) |
| Electric | $C$ | electric membrane capacitance | 1 μF/cm | Standard value (20) |
| | $R_i$ | cytoplasm resistivity | 0.25 kΩ cm | (19) |
| | $g_c$ | coupling conductance between dendrites and soma | 2.5 μS | Estimated |

**Table 2. Geometric, electric and internal Ca regulation parameters.**

**Synaptic currents**

MF activate GC whom axon, PF, makes excitatory synapses on PC spiny dendrites. Each PC receives inputs from large (> $10^5$ in rats (71)) arrays of PF. However, PF also activate SC, which make inhibitory synapses on PC. Thus, PC receive inputs from MF through a feedforward inhibition network whose overall effect varies between inhibition and excitation (72, 73). As the detailed activity in this network remains poorly documented and because of the very large GC/PC ratio (1), our model assumes a parsimonious description of the MF system into which it carries a tonic background input to PC (see e.g., (74)). On the opposite,

CF fire at a low frequency (~1 Hz), carrying phasic inputs to PC. Classical theories of the cerebellum suggest that the MF system may also signal brief, salient sensory-motor events through synchronous activation of PF/SC subsets, providing another source of phasic input to PC (75, 76). The phasic, $I_{\varphi}$ and tonic, $I_{dc}$ components of synaptic currents can be respectively regarded as signaling salient sensori-motor events and their context of occurrence. Phasic currents are modeled as bi-exponential functions

$$I_i(t) = g_i\left[1-\exp\left(-t/\tau_o\right)\right]\exp\left(-t/\tau_c\right)\left(E_i - V\right), \tag{SI7}$$

where $\tau_o$ and $\tau_c$ (ms) respectively stand for opening and closing time constants, the maximum conductance and inversion potential being respectively denoted by $g_i$ and $E_i$, with $i \in \{PF, CF, SC\}$. We take $\{2.4, 6.3\}$ (ms) and $\{0.9, 9\}$ (ms) for $\{\tau_o, \tau_c\}$ of PF and SC currents respectively (77, 78) and $\{0.7, 6.4\}$ (ms) for the CF current (79). $E_i$ is 0 mV for PF and CF currents (79) and –80 mV for SC currents (35). The value of $g_{CF}$ is 1.2 µS, consistent with the estimated value obtained from a multi-compartmental model (14).

We will submit codes of our model to modelDB after publication of this article.

***Model of the PC soma***

The conclusion that dendritic plateaus invade the entire cell, derived from equivalent cable model and supported by simulations of a detailed PC, agrees with recordings of Ca plateaus in the soma after blocking its Na channels (3). Our analysis suggests that dendritic signals can accordingly drive lasting transitions in the soma voltage between down (~–53 mV, valleys) and up (~–45 mV, plateaus) limits. Two recent studies (17, 33) have demonstrated that the SS threshold lies in the $[-48.9, -41.5]$ (mV) range of somatic voltages in adult PC. The partial overlap between these two voltage ranges confirms the soundness of investigating the hypothesis that dendritic signals decide epochs of firing/pauses from PC.

In order to correctly address this hypothesis, we needed a reliable model of the PC soma capturing its private dual electroresponsiveness. A recent study (18) documents capabilities of a simplified model to reproduce bistability, spontaneously resetting plateaus and type II firing properties of PC. However, this model produces only stable limit cycles and therefore fails providing a mechanism for Na plateaus. Moreover, it hypothesizes that dendrites bring a crucial contribution to the soma bistability through a slowly activating K current (activation time constant $\tau$ = 15ms). Experimental data are unable to substantiate this hypothesis because, in PC, purely voltage-dependent K current have exceptionally fast activation kinetics ($\tau$ < 1ms, (50)) and Ca-activated K channels also activate faster than the slow K current in (18) (59, 64). Our previous study (11) concluded that a transient balance between $I_{CaP}$ and the outward rectifying $K^+$ current of PC ($I_{Ksub}$ in our model, (45, 46, 51)) likely underlies spontaneously resetting dendritic $Ca^{2+}$ plateaus. We therefore designed a simple soma model to investigate the hypothesis that a similar interaction between $I_{Ksub}$ and the Na current, $I_{Na}$, may underlie Na plateaus. This model was simply obtained by substituting the experimentally-derived model of $I_{Na}$ in PC (56) for $I_{CaP}$ in the G&D model.

The model produces spontaneously resetting $Na^+$ plateaus with superimposed SS outlasting their triggering stimulus (inset in Fig. $1E_3$). Simulations show that zeroing the resurgent component current of $I_{Na}$ or removing $I_{Ksub}$ in the model prevents it to produce $Na^+$ plateaus. Together, these findings support the (i) hypothesis that the resurgent current of Na channels carries the depolarizing current during $Na^+$ plateaus (54) and (ii) conclusion that these plateaus results from distortions of the vector field at the left of a bistable range of $I_{dc}$. This shows that a similar balance between $I_{Ksub}$ and an inward current can explain both $Ca^{2+}$

and $Na^+$ plateaus potentials of PC. However, Na plateaus are labile signals in the model: they are only observed inside a narrow $I_{dc}$ range $[-72.1, 73.1]$ ($nAcm^{-2}$) and triggering of these signals is challenged by <1% changes in the stimulus amplitude (not illustrated), which can account for the scarce documentation of Na plateaus.

## II. Robustness of the model

PC exhibit stereotyped electric signals, like Ca-dependent plateaus and spikes despite significant variations in densities and activation parameters of ion channels from cell to cell. The present biophysical model therefore had to be robust to such fluctuations to propose a relevant mechanism for spikes and plateaus/valleys.

All results in this study are robust to large deviations in parameter values of the model (not illustrated). Moreover, the model retains its overall properties when other active currents found in PC are added to its basic formulation. However, simulations of these variant models suggest that the $I_h$, $I_A$ and $I_{KCa}$ currents found in PC might contribute to the shaping of dendritic plateaus and valleys.

Addition of the hyperpolarization-activated cationic current, $I_h$, to the basic model exerts opposite effects on its dynamics. On the one hand, the model retains its Ω zone (Fig. SM2-1A left) and the capability to produce plateaus and valleys (not shown) with low values of this current conductance, $g_h$ (i.e. in the order of that of $g_{Ksub}$). Nevertheless, increasing $g_h$ continuously decreases the Ω width up to the limit value $g_h$ = 183.85 μS/cm$^2$, where bistability is lost. This effect results from the small depolarizing contribution of $I_h$ at negative $V$, as evidenced by the upward shift of the model's resting potential (not illustrated). Our simulations therefore show that $I_h$ cannot be causal in the dendritic bistability, in agreement with the experimental observation that $I_h$ tends to mask bistability in PC (7). Nevertheless, responses of the $I_h$-endowed model to square pulses of hyperpolarizing currents suggest that moderate levels of $I_h$ can favor R → P dendritic transitions (Fig. SM2-1A right). Thus, with the example of $g_h$ = 30 μS/cm$^2$ (same value as the standard $g_{Ksub}$) the $I_h$-variant model still produces the whole spectrum of triangular to rectangular plateaus in response to depolarizing $I_\varphi$ (not illustrated). However, a transient rebound depolarization occurs at the break of hyperpolarizing $I_\varphi$. The rebound amplitude grows with that of the stimulus, as larger hyperpolarizations allow deinactivating larger $I_h$ fractions (Fig. SM2-1A right). The rebound can become so large that it paradoxically allows the hyperpolarizing input to trigger a plateau potential.

We did not attempt to evaluate the impact of slowly inactivating $I_A$-like currents on the model as these currents are absent in adult PC (80). Nevertheless, we simulated the impact of the subthreshold $I_A$ current studied by Sacco and Tampia (69) because its voltage dependence and inactivation time constant closely match those of the $I_A$ documented by Wang and Schreurs (81) in adult PC. Adding this current to the model neither prevents the occurrence of the Ω zone nor that of its companion plateaus and valleys (Fig. SM2-1B left). However, $I_A$ shifts the model's resting potential downward due to the 'window' hyperpolarizing current produced by the overlap between activation and inactivation curves of $I_A$ (69, 81).

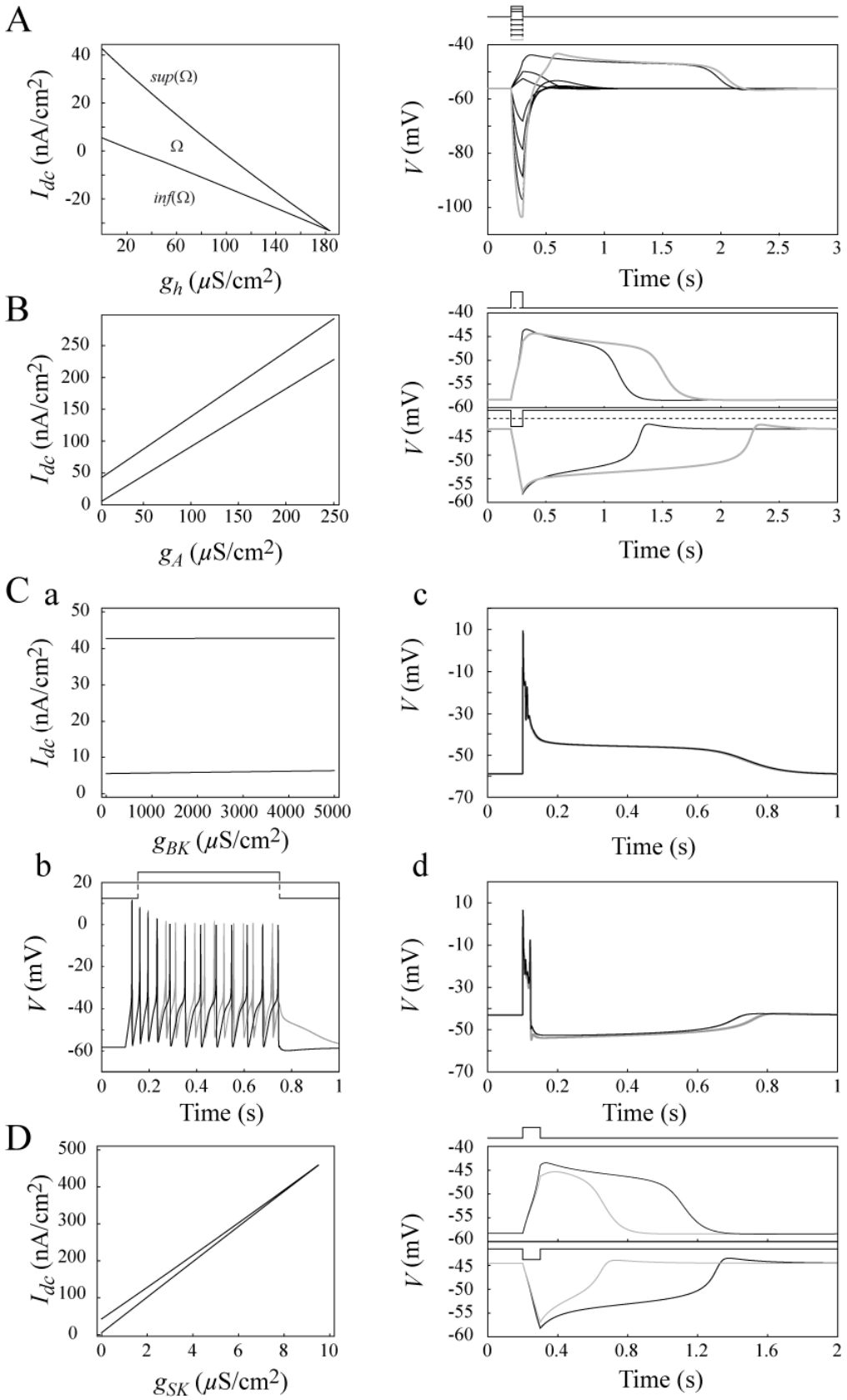
A
B
C a
b
c
d
D
sup(Ω)
Ω
inf(Ω)
$I_{dc}$ (nA/cm$^2$)
$g_h$ ($\mu$S/cm$^2$)
$g_A$ ($\mu$S/cm$^2$)
$g_{BK}$ ($\mu$S/cm$^2$)
$g_{SK}$ ($\mu$S/cm$^2$)
V (mV)
Time (s)

Figure SM2-1

**Fig. SM2-1 Robustness of the model to recently characterized currents in PC**. **A-D** Left (except panel **Cb**): impact on Ω of several conductances not introduced into the basic model. Right: responses of the basic model and its variants to hyper/depolarizing current pulses (illustrated on top of panels). **A** $I_h$ ($g_h$ = 30 μS/cm$^2$). A large hyperpolarizing pulse (-1250 nA/cm$^2$, grey trace) allows the rebound depolarization at pulse break to trigger a lasting plateau. **B** Reponses in the absence (dark traces) and with $I_A$ ($g_A$ = 30 μS/cm$^2$). **Cc** superimposed responses of the model in the absence (black trace) and with $I_{BK}$ (grey trace, $g_{BK}$ = 1250 μS/cm$^2$) to a 800 nA/cm$^2$ pulse of depolarizing current. **Cc&d**: impact of $I_{BK}$ on responses of the somatofugal cable to a CF input with dendrites initially in the R state (**c**, $I_{dc}$ = -25 nA/cm$^{-2}$) or P state (**d**, $I_{dc}$ = 45 nA/cm$^{-2}$). **D** Superimposed responses of the model lacking (black trace) and endowed with $I_{SK}$ ($g_{SK}$ = 2.5 μS/cm$^2$). $I_{dc}$ was adjusted to have the same resting potential in the two model versions: 0 (no $I_{SK}$) and 91.8 (with $I_{SK}$) (top panel, plateaus); 50 (no $I_{SK}$) and 176.18 (with $I_{SK}$) (bottom panel, valleys).

As a consequence, the Ω zone occurs at progressively larger $I_{dc}$ with increasing $g_A$ values, its width being however weakly sensitive to large $g_A$ changes (Fig. SM2-1B left). Given the voltage–sensitivity of plateau/valley signals, we achieved a faithful evaluation of the $I_A$ contribution to dynamics of these signals by comparing responses of the basic and $I_A$-endowed models. The latter one was fed with a constant current to insure a same resting potential in the two model versions. Fig. SM2-1B (right panel) illustrates potent effects of $I_A$ to lengthen both plateaus and valleys predicted by the basic model. The plateau's lengthening results from $I_A$ inactivation upon depolarization, which shifts the balance of membrane ion currents toward the depolarizing, non-inactivating $I_{CaP}$. On the opposite, deinactivation of $I_A$ upon hyperpolarization is responsible for the lengthening of valleys as it shifts the current balance toward K currents.

We also examined the effects of introducing Ca-activated K (KCa) channels into the model as they carry a significant fraction of the total K current in PC (43). Plateaus, valleys and bistability in the model are largely robust to the inclusion of $I_{BK}$ (Fig. SM2-1Ca). Thus, this current neither affects width of the Ω zone nor plateau-valley duration/$I_{dc}$ relations (not illustrated), even with conductances as large as that of $I_{Kdr}$. A plateau shortening of less than 5% is only observed with unrealistically large conductance densities of $5\times10^3$ μS/cm$^2$ (data not shown). This result is readily understood from the large (several μM) Ca elevations required to activate BK channels of PC, their half-activation potential remaining positive at high Ca levels (59). $I_{BK}$ is thus unable to affect plateau and valley signals, which involve sub-micromolar Ca variations over a ~ –60 to –40 mV range of membrane potentials. However, Ca spikes induce micromolar Ca elevations in dendrites (25) which are large enough to significantly activate BK channels (57, 58). In response to large depolarizing driving currents, repetitive firing of Ca spikes thus occurs at lower frequencies in the model with BK channels (Fig. SM2-1C left). Moreover, each Ca spike exhibits a larger after-hyperpolarization (AHP;). This is consistent with the finding that blocking BK channels reduces the Ca spikes AHP (57) and increases the frequency of Na-Ca bursts (82).

By contrast to BK channels, simulations of a variant model including SK channels found in PC suggest a prominent role for these channels in PC dendrites plateaus/valleys. Thus, a conductance density of 1 μS/cm$^2$ (i.e. several orders of magnitude smaller than that of $I_{Kdr}$ and $I_{Ksub}$) significantly narrows the Ω zone (Fig. SM3-1D left). Bistability vanishes for $g_{SK}$ > 9.5 μS/cm$^2$, i.e. the third of $g_{Ksub}$. This prominent effect results from the downward shift of its resting potential due to the significant activation of SK channels at resting Ca levels. We adopted the same strategy as with $I_A$ to compare plateau/valley dynamics in the SK-variant and canonical versions of the model. Starting from the same membrane potential, a 100 ms

duration depolarizing pulse triggers a shorter duration plateau in the SK-endowed model than in its canonical version (Fig. SM3-1D right). Similarly, a hyperpolarizing pulse triggers a shorter valley in the SK-endowed model than in the basic model. These effects results from the addition of the hyperpolarizing current of SK channels to that of $I_{Kdr}$ and $I_{Ksub}$. Upon a depolarizing pulse, $I_{CaP}$ activates so that $[Ca]_i$ increases during the plateau, which activates SK channels. $I_{SK}$ adds to $I_{Kdr}$ and $I_{Ksub}$ to shorten the plateau. On the opposite, $[Ca]_i$ decreases during valleys, partially deactivating $I_{SK}$ and thereby shifts the total membrane current in favor of $I_{CaP}$, which shortens valleys.

Despite a thorough exploration of its parameter space, our model proves unable to reproduce the *in vitro* trimodal activity pattern of PC (tonic SS firing epochs, followed by Na-Ca bursts and ended by pauses lasting for dozens of seconds (83)). Inability of our model to reproduce this pattern should not be considered as a limitation because this pattern was only observed in a subset of available data and CF activation at physiological frequencies restores the *in vivo*-like pattern of activity of the cell (84).

Experiments have not yet identified the outward rectifying $K^+$ current in isolated cell bodies (68), suggesting that this current may be segregated to dendrites. We therefore investigated whether the Na plateau mechanism described in SMI also holds in the entire cell with the somatic compartment lacking $I_{Ksub}$. Fig. SM2-2 illustrates the soma voltage time course in response to 150 ms depolarizing pulse (0.4 nA amplitude, current injected in the soma compartment). $I_{CaP}$ was zeroed to reproduce conditions in which $Na^+$ plateaus were identified by Llinás and Sugimori (2). The illustration shows how the depolarizing pulse triggers a lasting Na plateau ($I_{dc}$ = 0.34 nA in the soma, no tonic current in dendrites). This result stems from the fact that the somatic depolarization during repetitive SS firing activates $I_{Ksub}$ in the dendrites through the dendro-somatic electric coupling.

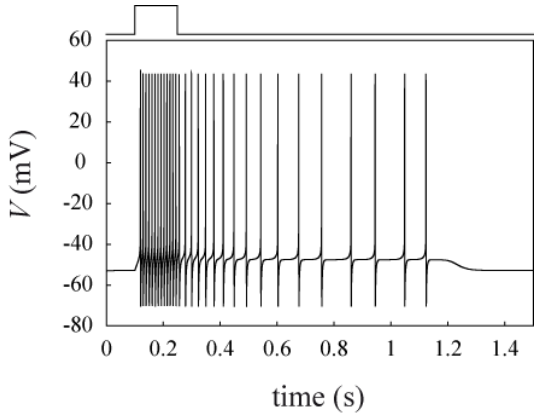


Figure SM2-2

Illustrated results in the main text were obtained by assuming a uniform $I_{Ksub}$ distribution over the somato-dendritic membrane. Further experiments are required to evaluate a possible segregation of $I_{Ksub}$ to dendrites which may contribute setting the plateau/valley-duration / $I_{dc}$ relation.

# III. Simplified representations of the PC architecture

***The infinite cable***

Simulating the extended model in infinite cables offered a convenient way to investigate intrinsic capabilities of dendritic PC plateaus/valleys to propagate waves of electric signals using the G&D mechanism. In such unbounded domains, electric waves travel without shape changes with a uniform speed, $\theta$. The existence of such wave solutions in the model could accordingly be proven by rewriting PDE in a co-moving frame of reference, with coordinate $\xi = x - \theta t$, accompanying the wave propagation in the positive *x*-direction (85). After this coordinate change, the model reads as a system of ODE

$$\frac{dV}{d\xi} = V_\xi, \tag{SIII1-A}$$

$$\frac{dV_\xi}{d\xi} = \frac{2R_i}{R_d}\left(-C\theta V_\xi + I_{ion} - I_{dc}\right), \tag{SIII1-B}$$

$$\theta\left[1 + \frac{[B]_T / K_d}{\left(1 + [Ca]_i / K_d\right)^2}\right]\frac{d[Ca]_i}{d\xi} = \frac{10^{-9} I_{Ca} R_d}{F\delta\left(2R_d - \delta\right)} + \frac{2k\left([Ca]_i - [Ca]_b\right)\left(R_d - \delta\right)}{\delta\left(2R_d - \delta\right)}, \tag{SIII1-C}$$

, (SIII1-D)

with the additional parameter $\theta$. Eqs. SIII1 are referred to as the 'traveling system' in Results. Propagated waves appear in this frame as standing voltage profiles connecting a resting point of Eqs. SIII1 to itself (homoclinic orbits) or two different resting states (heteroclinic orbits) (86). Fig. SM3-1 relates orbits searched for in the co-moving frame to their counterparts in the space domain (i.e. voltage profiles along the dendrite at a given instant). Fixed points in the traveling system correspond to a uniformly polarized dendrite (spatially uniform steady state). Heteroclinic orbits connecting two steady states correspond to traveling fronts, whereas homoclinics to a single steady state translate into traveling pulses, representing either finite duration plateaus/valley potentials, Ca spikes or a combination of both. The key problem of our computations was to find $\theta$ values allowing for homo- and heteroclinic orbits to occur in order to prove the existence of the corresponding traveling waves. Homo- and heteroclinics were searched for with the Homcont set of numerical routines (87) imported by B. Ermentrout into his XPP software (www.pitt.edu/~phase). These numerical methods can only approximate homo- and heteroclinics as they necessarily work on finite time intervals, whereas dynamical systems take an infinite time to travel along these orbits. Owing to this limit, algorithms in Homcont refine an initial approximation of these orbits by extending it along a parameter $\Pi$ multiplying the right-hand side of Eqs. SIII1. Illustrated homo- and heteroclinics were computed with $\Pi$ = 50. We verified that $\Pi$ values a hundred-time larger did not change results significantly. These results were cross-validated by simulating the model in cables several times longer than the orbit wavelength (in order to make boundary effects negligible and thus approximate the infinite dendrite case) to guarantee that illustrated orbits (Figs. 2) represent reliable approximations of true homo- and heteroclinic solutions of the model. These simulations were performed with a home-made code implementing the semi-implicit Crank-Nicholson formulation (88) of the model equations with sealed-end boundaries; the set of non-linear algebraic equations resulting from the spatial discretization of Eqs. 1-3 was solved at each time-step by Gauss-Seidel elimination (89).

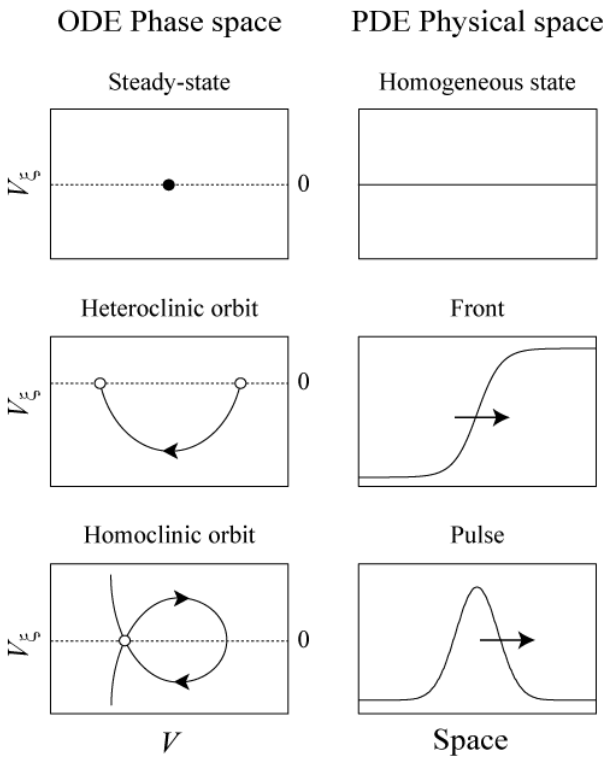


Figure SM3-1

An exhaustive exploration of (homo-)heteroclinic solutions of Eqs. SIII1 was elusive because this system is 4-dimensional. By contrast, the existence of (homo) heteroclinics can be proved geometrically in 2D dynamical systems: manifolds of fixed points are one-dimensional (i.e. lines) and it can be easily verified in the phase plane whether or not they can produce (homo) heteroclinic connections. For this reason, we derived a 2D simplified version of the model by assuming instantaneous activation of $I_{Kdr}$ and rapid equilibrium of $[Ca]_i$. These simplifying assumptions are justified by the fact that plateaus/valleys are slow electric events compared to the rate of activation of $I_{Kdr}$ (the largest value of its voltage-dependent time constant is 2.9 ms) and our previous study has demonstrated that the homogeneous model retains the capability to produce plateaus/valleys with $[Ca]_i$ set at its equilibrium value at each point in time (11). Introducing these two simplifications, the traveling system reduces to the following set of differential-algebraic equations:

$$\frac{dV}{d\xi} = V_\xi \tag{SIII2A}$$

$$\frac{dV_\xi}{d\xi} = \frac{2R_i}{R_d}\left(-C\theta V_\xi + I_{ion} - I_{dc}\right) \tag{SIII2B}$$

$$10^{-9} I_{Ca} R_d / F + 2k\left(\left[Ca\right]_i - \left[Ca\right]_b\right)\left(R_d - \delta\right) = 0 \tag{SIII2C}$$

With the example of $R_d$ = 0.5 µm, an approximate solution of implicit Eq. SIII2C (best non linear fit obtained with the Levenberg-Marquardt algorithm (89)) is given by

$$[Ca]_i(V) = 5\times10^{-2} + 10^{-2}/\exp\left(-(V+66)/5\right).$$

Substituting this solution for [*Ca*]*i* in Eq. SIII2B, the traveling system reduces to a system of two ODE with variables $V$ and $V\xi$, subsequently referred to as the '2D model', which captures the essential characteristics of the full model in the voltage range below the Ca spike threshold.

***Equivalent cable representations of PC dendrites***

PC dendrites exhibit a dichotomous pattern of branching: the primary dendritic trunk splits into two daughter branches with approximately identical diameters and so on (clearly visible in the PC reconstructed by Shelton (19) illustrated in Fig. SM3-2A; also see (1)). Exceptions occur at spiny branchlets whose initial segment has a smaller diameter than their parent smooth dendrite. The variable lengths of dendritic segments and termination of dendritic branchlets after random numbers of branch points explain the various cell shapes observed in the PC population (1). Theoretical studies have shown that propagation of an action potential in an excitable dendritic tree with uniform ion channel densities is more secure in the somatofugal direction (from soma to dendrites) than in the somatopetal direction (see e.g., (90)). Moreover, Stockbridge (91) has demonstrated that an action potential reaching a branch point where a segment splits into two daughter segments with identical diameters but unequal lengths (like in PC dendrites) cannot invade the longer branch without invading the shorter one (Fig. SM3-2B). We could thereby put that an active electric signal (i.e. spike or plateau) triggered close to the soma cannot reach the tip of the longest branch in the tree (in electrotonic units) without invading all other branches. The situation was somewhat different for an active signal triggered in distal dendrites (Fig. SM3-2B), which has first to reach the soma before possibly invading the rest of the cell. From the excited branch, the signal propagates more easily in sister branches than in the parent trunk because the latter has a larger diameter and the rest of the tree imposes a huge current sink, decreasing efficiency of the axial current to depolarize the trunk beyond the voltage threshold. This effect prevents diameter differences at spiny/smooth dendrites branch points to challenge our previous conclusion regarding somatofugal propagation. Moreover, it entails that centripetal propagation to the soma implicates propagation in all branches encountered along the path connecting the excitation site to the soma. For propagation beyond the soma in the rest of the tree, we retrieve the somatofugal case discussed above.

From the above analysis, we concluded that a necessary and sufficient condition for an active electric signal to invade a whole PC is the propagation of this signal along the longest electrotonic path connecting its locus of origin to dendritic tips, whatever its location in the cell. We deduced from this condition that an equivalent cable model of PC reproducing electrotonic attenuation along this path is sufficient to investigate whether dendritic Ca-dependent plateaus and spikes can invade the whole dendritic tree. However, no single equivalent cable can possibly allow investigation of both somatofugal and somatopetal propagation of these signals at the same time since attenuation of electric signals is asymmetric in dendrites, being much steeper in the centripetal direction (92). We therefore built two types of equivalent cables respectively aimed at simulating the somatofugal propagation of spikes of plateaus/valleys triggered by the CF (Fig. SM3-2$C_{1\text{-}3}$) and somatopetal propagation plateaus/valleys triggered by PF and SC (Fig. SM3-2$D_{1\text{-}3}$). Their physical dimensions were adjusted to reproduce the total surface and input resistance of the full Shelton's PC.

The general algorithm for building somatofugal and somatopetal equivalent cable representations of Shelton's PC was as follows. Having chosen a locus of synaptic input, we

first computed the electrotonic attenuation of this input at every dendritic termination of the tree endowed with a passive leakage conductance, $g_L$, using the iterative method of Rall (93). The path with the longest electrotonic length from the input location, $L_{max}$, was selected in the resulting dendogram (Fig. SM3-2C$_1$). A straight cable comprising $n$ cylindrical segments with identical electrotonic length, $L_{\max}/n$, but varying radii, $R_{ci}$ ($i$=1..$n$), producing the same electrotonic attenuation was then built as follows. Radius of the more distal segment, $R_{cn}$, being set to an initial guess value, the voltage profile along the equivalent cable was analytically expressed with Rall's method. The voltage values at the termination of the $n$–1 remaining segments depending on the $n$–1 unknown radii were then equated to the corresponding values computed along the longest electrotonic path in the tree. This resulted in a set of $n$–1 non-linear algebraic equations, which was solved iteratively by varying $R_{cn}$ until the total membrane surface and input impedance of the equivalent cable approximately matched those of the uncollapsed dendritic tree. We found impossible to find a single set of radii reproducing exactly the two parameters value at the same time, either for the somatofugal or somatopetal cables. We selected parameter sets representing the most appropriate tradeoff between these constraints, according to the respective question investigated with the two kinds of cables.

In the case of the somatofugal cable, we selected a set of radii for which the total membrane surfaces of the equivalent cable and uncollapsed dendritic tree matched because the CF achieves multiple synapses on smooth dendrites (hence its effect does not depend on the somatic input resistance). The best fit 'somatofugal model' had a 73.5 µm diameter for its most distal segment and a total membrane area of $4.1 \times 10^5$ µm$^2$ (0.6% difference with the membrane area of the full cell). The somatic input resistance was 33% larger than the value in the uncollapsed cell. The cable had an electrotonic length of 0.55, close to values documented in previous studies (0.57 (38) and 0.59 (94)). On the opposite, the input resistance of the excited branch was chosen to constrain radii of somatopetal cables since this factor crucially determines conduction toward the soma of active electric signals triggered in a neuron's dendrites (90). For example, the best-fit somatopetal equivalent cable model (Fig. SM3-2D$_3$) had a terminal radius of 511 µm and an input resistance of 52 MΩ at the origin of branch 68 (0.7% difference with the value in the uncollapsed tree) selected as the target of synaptic inputs (see below). The membrane surface was however ~1.5 that of the actual cell, so that conductances values for exciting plateau and valleys derived using this model (Fig. 3C) must be regarded as superior bounds.

In the case of somatopetal cables, the branchlet receiving synaptic inputs was fully described and connected to the lumped tree, in order to investigate the impact of different distributions of synaptic input onto this branch. The illustrated results were obtained with branch 68 (using Shelton's indexation, see Fig. 3 in (19)) as the site of distal inputs. Additional simulations in which synaptic inputs were targeted to different branches (69 and 85) gave similar results. Segments in a spiny branch were numbered as follows: the initial segment, labeled n°1, divides in two ramifications. N°2 was given to the segment of the ramification producing the least number of further ramifications and so on. Upon reaching a terminal segment, numbering resumed to the parent segment.

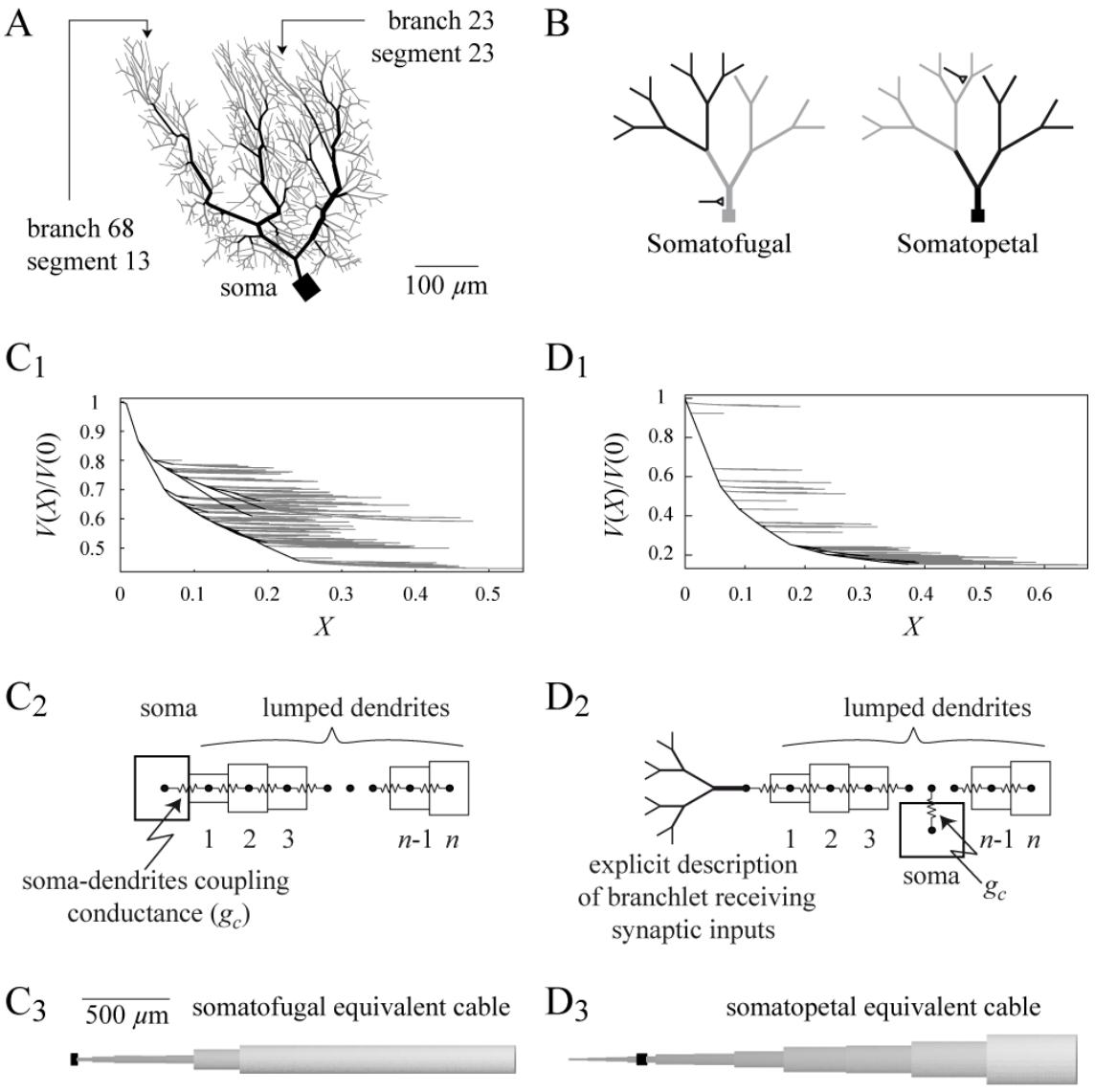


Figure SM3-2

This algorithm was applied to Shelton's PC after a dual rescaling of its geometrical dimensions. Following Shelton (19), we first multiplied length $l$ and radius $R_d$ of each dendritic segment by 1.36 to obtain the larger physical dimensions of a guinea pig PC, for which Shelton provided estimations of $g_L$ and $R_i$ used as standard values of these parameters in our study. PC have impressive numbers of synaptic boutons that bring an extra membrane surface to 'nude' dendrites. As the membrane of spines represent > 75 % of the total cell surface (31), we further rescaled geometrical parameters of Shelton's cell to complete a realistic picture of its actual dimensions, using the method of Segev et al. (95). Finally, thickness $\delta$ of the cytoplasmic shell in the two reduced models was rescaled at each electrotonic distance from the locus of synaptic input to preserve surface/volume ratios in the full cell and thereby ensure realistic $[Ca]_i$ dynamics.

Impact of the CF input on Shelton's PC was simulated with the somatofugal cable as follows. The conductance $g_{CF}$ (μS) was uniformly distributed over all proximal compartments of the cable closer to the soma (in electrotonic units) than the farthest smooth segment in the uncollapsed cell.

*Endowing equivalent cables with an excitable soma*

A major goal of our study was to investigate the hypothesis that dendritic Ca signals command the SS output of PC. Owing to the well known somatic/dendritic segregation of Na/Ca channels, addressing this question required connecting a soma model to the lumped dendritic trees. The soma was modeled as an isopotential compartment, which was electrically connected to the dendrites by adding a coupling current to the soma voltage, $V_s$, equation (96)

$$C\frac{dV_s}{dt} = -\left(I_{Na} + I_{Kdr} + I_{Ksub} + I_L\right) + \frac{g_c}{q}\left(V_d - V_s\right), \qquad \text{(SIII3)}$$

where $q$ denotes the ratio of the somatic membrane area to the total cell membrane surface, $g_c$ (μS/cm$^2$) the dendrites-soma coupling conductance and $V_d$ the membrane voltage of the dendritic compartment in lumped trees which is connected to the soma. For the somatofugal cable, this compartment was the first one of the cable (Fig. SM3-2C$_2$). For somatopetal cables, the electrotonic distance of the soma from the excited branch was localized in the dendogram (Fig. SM3-2D$_2$) and the compartment localized at the corresponding distance in equivalent cables was selected as the connected compartment. Similarly, the balance equation of $V_d$ was supplemented by the coupling current $\frac{g_c}{1-q}\left(V_s - V_d\right)$. No analytical method has yet been developed to determine $g_c$ from the geometry of a neuron and electric parameters of its membrane. Nevertheless, we could easily constrain the $g_c$ value by demanding equivalent cable models to reproduce the characteristic Na-Ca spike bursts of PC (4). The only fibers targeting the PC soma are axons of basket cells, which are not included in our model (hence the absence of a synaptic current in Eq. SIII3) as its objective is to understand dendritic dynamics and their impact on SS firing. Besides, our simplified model of the soma does not include Ca currents, dispensing us to model Ca dynamics in the soma.

# IV. Dendritic control of somatic firing

Simulations of a somatopetal cable model provide direct evidence for a dendritic control of somatic firing in the soma as illustrated in Fig. SM4-1. The dendrites and soma of the model were initially uncoupled (i.e. by setting $g_c$ = 0) and the coupling conductance was step raised to its standard value. A variable tonic current was fed to the dendrites to determine their initial state, resting (A) or plateau (B). Our model of the isolated soma is bistable in the absence of synaptic inputs (Fig. 1E$_1$) in agreement with experimental data and its initial state was arbitrarily set to its silent (A) or firing (B) mode.

With the dendrites initially in their R state ($I_{dc}$ = -25 nA/cm$^2$) and a spontaneously firing soma, raising $g_c$ from zero to its standard value abruptly interrupts the somatic firing (A). By contrast, the dendritic membrane potential, $V_d$, undergoes no significant change. In the inverse situation where dendrites are initially switched to their plateau state ($I_{dc}$ = 45 nA/cm$^2$) and the soma initially quiescent, introducing the dendro-somatic coupling induces SS firing in the soma (B). No significant $V_d$ change either occurs in this situation.

These results evidence directly the dendritic control of somatic firing suggested implicitly by the bifurcation diagram illustrated in Fig. 4A$_1$. These results are consistent with

relative values of the coupling currents in the dendrites and the soma stemming from voltage differences between these two regions of the cell. Thus, according to the expressions for the density of these currents (SMIII), $I_C^s$ is ~20 times larger than $I_C^d$ with the standard $g_c$ and $q$ values (Table 2), which explains how dendrites in their plateau state can strongly depolarize the soma without the somatic firing significantly impacting on $V_d$.

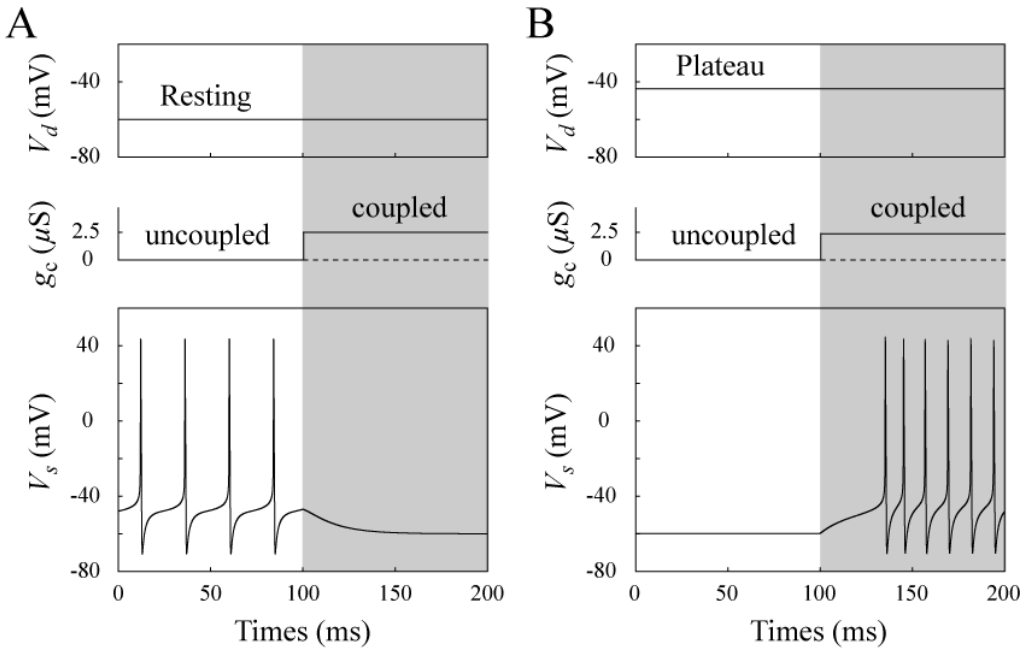


Figure SM4-1

**Fig. SM4-1 Responses of dendrites and soma of a somatopetal model to step introduction of the dendro-somatic electric conductance $g_c$ in an initially uncoupled model.** Notice that switches of the soma between its silent and firing modes induce no significant changes in the dendritic voltage, owing to the hoveringly large ratio of the dendrites/soma membrane ratio.

## V. Simulations of the plateau/valley mechanism in a fully reconstructed PC

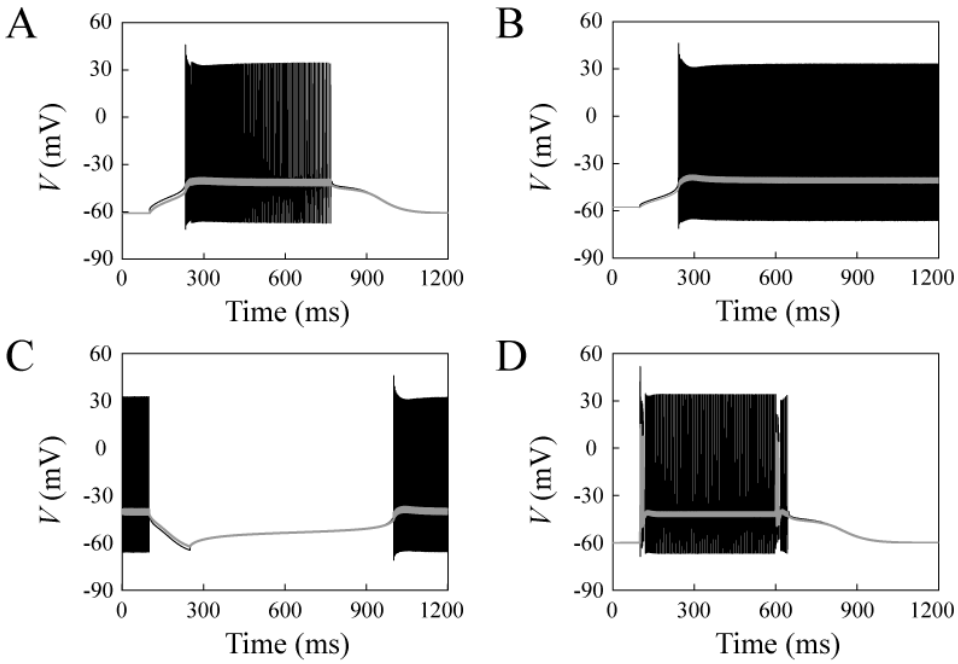


Figure SM5-1

**Fig. SM5-1 Simulation of the plateau mechanism in Shelton's PC (19) with the Neuron software.** Conductance densities were the same as in simulations of the model in equivalent cable except in the soma ($g_{Na} = 1.3\times10^5$ μS/cm$^2$, $g_{Kdr} = 2\times10^5$ μS/cm$^2$). Dark traces: somatic membrane potential, grey traces: membrane potential in a proximal spiny dendrite. **A** Response of the cell to an excitatory current delivered to the dendrites (0.55 nA, 150 ms) in the presence of a SC background synaptic conductance (2 μS/cm$^2$). **B** Same as **A**, with no background current. **C** Cell's response to an inhibitory dendritic current (-0.6 nA, 150 ms) in the presence of a PF background synaptic conductance (0.84 μS/cm$^2$). **D** Response to two successive CF inputs. The CF synaptic conductance (7 μS/cm$^2$) was uniformly distributed over smooth dendrites. The SC background conductance was 1.2 μS/cm$^2$.

## VI. Phasic inhibitory inputs control the valley duration

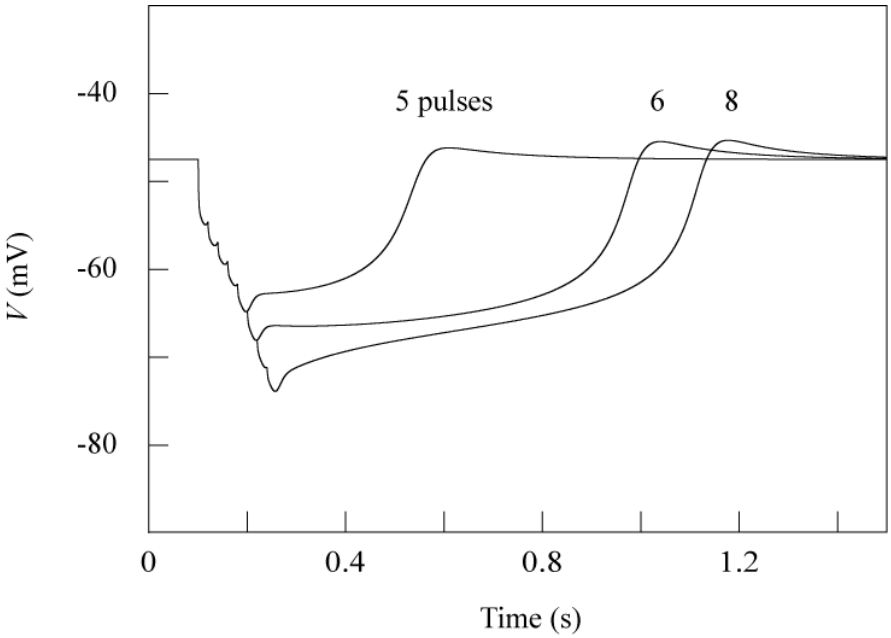


Figure SM6-1

**Fig. SM6-1 Responses of the standard somatopetal cable with passive soma to a variable train of SC inputs.** Traces illustrate the somatic membrane voltage. Synaptic parameters were the same as in Fig. $3B_4$ with $I_{dc}$ = 45 nA/cm$^2$. The valley duration increases non-linearly with the number of successive SC inputs, like the duration of pauses in PC firing (Fig. 3B in (17)).

## VII. Dendritic plateau and valley potentials represent an original mechanism of electric signaling in PC

Excitable cells have been shown to display only two electric signaling mechanisms (97): (i) passive conduction of electrotonii in cells with linear *I-V* relations and (ii) spike propagation in cells endowed with non-linear membrane properties. Spikes are traveling waves propagating without shape change in straight cables at a constant propagation speed. No such speed can be defined for an electrotonus (its magnitude decaying with distance from the excitation site) and physiologists have therefore introduced a pseudo-propagation speed termed 'conduction velocity'. We have thus reserved the term 'propagation' for traveling wave solutions in the usual mathematical sense and restricted the term 'conduction' to electrotonus. The reason for this clarification is that we provide evidence, based on simulations and theoretical considerations, that plateau and valley potentials represent an original mode of electrical signaling in PC displaying hybrid properties intermediate between that of action potentials and that of an electrotonus. We document below how this original signaling mechanism can emerge from the interplay between intrinsic and active membrane properties into the peculiar architecture of PC.

**Plateau potential are neither spikes not electrotonus**

In our model, plateaus exhibit a close to uniform amplitude over dendrites of Shelton's cell. Slight (<1mV) amplitude differences are however noticeable between smooth and spiny

dendrites which stem from their different radii. To precisely compute the conduction speed of the rising and decaying phases of plateaus in our equivalent cable or full cell models would thus necessitate preliminary renormalization of the voltage trajectories. To avoid these procedures, we simulated our model in a straight cable with a 0.5 μm radius and an electrotonic length $L$~1.

We first computed the speed of the rising phase of plateaus triggered by rectangular pulses of current, $I_\varphi$, injected at $X = 0$ and calculated the speed at the membrane potential $V$ = -53 mV (close to the voltage inflexion point of the plateau relaxation, which is used to compute the plateau duration).

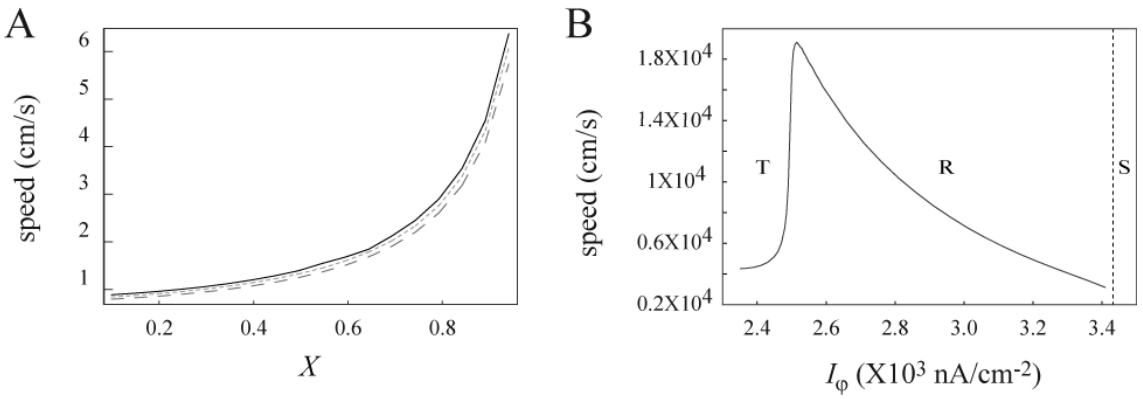


Figure SM7-1

**Fig. SM7-1 Simulation of the plateau mechanism in a straight cable with an electrotonic length L~1.** The cable was stimulated at its left end with square pulses of depolarizing current, $I_\varphi$, ($\times 10^3$ nA/cm$^2$, 150 ms duration): 2.8 (solid line), 2.65 dotted line and 2.5 (dashed line). **A** Conduction speed of the rising phase of the plateau as a function of the electronic distance $X$. **B** Conduction speed of the decaying phase of the plateau versus $I_\varphi$ calculated at the center of the cable. T, triangular plateaus, R rectangular ones, S spikes.

Fig. SM7-1A plots the speeds computed along the cable for three different $I_\varphi$ amplitudes. First notice that the curves are very similar despite plateaus displayed very different durations (not illustrated). Unlike that of the electrotonus, the conduction speed of the plateau rise increases monotonically with $X$, indicating the involvement of the membrane active conductances. However, the speed range remains close to the theoretical value for electrotonus conduction speed in a passive cable (1.41 cm/s with our settings, see (97), p. 34-35), showing that the travelling speed of the plateau rise is dominated by passive membrane properties.

We then computed the travelling speed, $v_f$, of the repolarizing phase of plateaus triggered by the same current protocols and at the same potential $V$ = -53mV. Fig. SM7-1B illustrates the minimum value of this speed (encountered approximately at the center of the cable where the effects of sealed ends are the lowest) as a function of $I_\varphi$. In contrast with the speed of the plateau rise, the speed of the plateau decay strongly depends on the amplitude of $I_\varphi$, in a non-monotonic fashion. However, in the entire range of $I_\varphi$ values capable to trigger plateaus, the decaying phase of plateaus travels at speeds which are at least three orders of magnitude larger than the speed of the rising phase.

Note that the same results were obtained from simulations with the Matlab, Maple and XPP softwares. This grants that the three orders of difference between the travelling speed of

the plateau rise and decay is an actual feature of our model and does not result from numerical errors. Simulations show, in a similar way, that valleys exhibit speeds of rise and decay differing by 2-4 orders of magnitude (not shown). Hence, the properties of dendritic plateau and valley potentials contradict the definition of a propagating traveling wave as a voltage trajectory where all points travel with a unique speed. We therefore conclude that plateau and valley potentials in PC dendrites can neither be classified as actively propagating spikes nor as passively conducted electrotonus.

**The mechanism of plateaus/valleys conduction**

In this section, we develop theoretical elements in order to more precisely understand this original conduction mechanism. Let us consider the response to a Dirac current input of a *passive* cable terminated at both ends by an open circuit. Dirac input is used here as a limiting case of the prolonged current stimulations that are used in our model to trigger plateau potentials. The response of this finite passive cable to such a Dirac input can be exactly computed as an infinite series of exponential terms (97)

$$V\left(X,T\right)=\frac{r_a\lambda Q}{2\tau_m}\frac{e^{-T}}{\sqrt{\pi T}}\sum_{n=-\infty}^{+\infty}e^{-\left(nL-X/2\right)^2/T}\ , \qquad \text{(SVII1)}$$

in which $X=x/\lambda$ and $T=t/\tau_m$ represent respectively the space and time variables normalized according to their respective constants $\lambda=\sqrt{R_d/2R_i g_m}$ and $\tau_m=C/g_m$; $L$ is the cable length in electrotonic units, $Q$ is the charge applied to $X=0$ and $r_a=R_i/\pi R_d{}^2$.

It actually takes a large amount of time before distant parts of the cable respond to the input so that this finite cable initially behaves as an infinite one ((97), p. 73). In other words, when the rising front occurs, sealed-boundaries have not yet influenced the cable. As a consequence, the conduction speed of the plateau rise is of the order of that of the electrotonus. At the end of this initial rising stage, the potential reaches ~ -45 mV. At this point, active ionic currents activate and take over the passive ones. This yields a prolonged plateau phase, which is an emergent property of the interplay between active currents. Furthermore, a constant voltage, long-lasting signal (i.e. the plateau phase itself) adds to reflection currents at sealed ends to render the cable isopotential at long times.

Finally, Eq. SVII1 also allows explaining the very large values of $v_f$. Indeed, it predicts that the travelling speed of the repolarization part of an electrotonus increases exponentially fast with $T$ (not shown). Hence the larger is the plateau duration ($d$), the larger is the conduction speed of the repolarization front. In the case where active current provoke a long plateau phase before the onset of repolarization, this analysis predicts that the propagation speed of the plateau foot should reach huge values. This is exactly what is observed in our simulations in the full cell and equivalent cable: when repolarization is delayed by the long duration of the plateau phase, $v_f$ reaches extremely large values (Fig. SM7-1B).

The resulting conduction mechanism can be summarized as follows. The plateau rise phase is mostly due the passive membrane properties, hence its slow conduction speed. The plateau phase then develops and the conjunction between long-lasting plateaus and sealed-end boundaries homogenizes the membrane potential over the whole dendritic tree. Finally, the speed of the repolarization front increases with $d$ in a supralinear manner, yielding huge propagation speeds.

To test this interpretation, we ran further simulations of our model in the straight cable considered in the above section. Fig. SM7-2A confirms that $v_f$ exponentially depends on $d$, much like the repolarization speed increases exponentially with $T$ in a passive cable: branches

of points corresponding to rectangular (R) and triangular (T) plateaus plotted in log-linear scale are well fitted by two lines with respective slopes 4.3 and 13.8. The slope difference results from the conjunction of two factors, which can be understood after rewriting $v_f$ as a function of the membrane electric parameters, i.e. $v_f = \sqrt{\frac{R_d g_m}{2 R_i C^2}} \frac{\Delta x}{\Delta t}$. On the one hand, the $I_{CaP}$, $I_{Ksub}$ and $I_{Kdr}$ currents are more activated during R than T plateaus, resulting in a ~2 times larger $g_m$ value during T plateaus. On the other hand, the repolarization rate ($dV/dt$) of T plateaus is larger than that of R ones, resulting in larger speeds $\Delta x/\Delta t$ for the former kind of plateaus (Fig. SM7-2B). The combination of these two effects is responsible for the larger slope of the R plateaus line in Fig. SM7-2A. Taken together, these results corroborate our interpretation and support the conduction mechanism we expose above for dendritic plateaus and valleys.

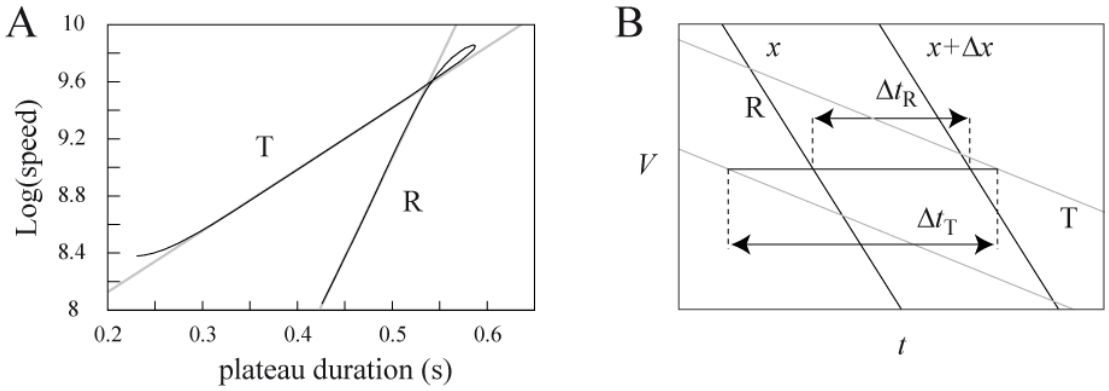


Figure SM7-2

**Fig. SM7-2 Mechanism of plateaus conduction. A.** The travelling speed, $v_f$, of the decaying phase of plateaus illustrated in Fig. SM7-1B is plotted as a function of the plateaus duration in log-linear coordinates. Grey lines represent the best result of two linear regressions of the points corresponding to triangular (T) and rectangular (R) plateaus. **B**. Diagram illustrating how a larger repolarization rate d$V$/d$t$ contributes to increase the slope of the T plateaus line with respect to that of R ones in **A**.

## SUPPLEMENTARY REFERENCES


**38.** **De Schutter, E., and J. M. Bower. 1994. An active membrane model of the cerebellar Purkinje cell II. Simulation of synaptic responses. J Neurophysiol 71:401-419.**

**39.** **Mintz, I. M., V. J. Venema, K. M. Swiderek, T. D. Lee, B. P. Bean, and M. E. Adams. 1992. P-type calcium channels blocked by the spider toxin omega-Aga-IVA. Nature 355:827-829.**

**40.** **Gahwiler, B. H., and I. Llano. 1989. Sodium and potassium conductances in somatic membranes of rat Purkinje cells from organotypic cerebellar cultures. J Physiol (Lond) 417:105-122.**

**41.** **Gruol, D. L., T. Jacquin, and A. J. Yool. 1991. Single-channel K+ currents recorded from the somatic and dendritic regions of cerebellar Purkinje neurons in culture. J Neurosci 11:1002-1015.**

**42.** **Regan, L. J. 1991. Voltage-dependent calcium currents in Purkinje cells from rat cerebellar vermis. J Neurosci 11:2259-2269.**

**43.** **Raman, I. M., and B. P. Bean. 1999. Ionic currents underlying spontaneous action potentials in isolated cerebellar Purkinje neurons. J Neurosci 19:1663-1674.**

**44.** **Watanabe, S., H. Takagi, T. Miyasho, M. Inoue, Y. Kirino, Y. Kudo, and H. Miyakawa. 1998. Differential roles of two types of voltage-gated Ca2+ channels in the dendrites of rat cerebellar Purkinje neurons. Brain Res 791:43-55.**

**45.** **Etzion, Y., and Y. Grossman. 1998. Potassium currents modulation of calcium spike firing in dendrites of cerebellar Purkinje cells. Exp Brain Res 122:283-294.**

**46.** **Etzion, Y., and Y. Grossman. 2001. Highly 4-aminopyridine sensitive delayed rectifier current modulates the excitability of guinea pig cerebellar Purkinje cells. Exp Brain Res 139:419-425.**

**47.** **Genet, S., and R. T. Kado. 1997. Hyperpolarizing current of the Na/K ATPase contributes to the membrane polarization of the Purkinje cell in rat cerebellum. Pflugers Arch 434:559-567.**

**48.** **Martina, M., G. L. Yao, and B. P. Bean. 2003. Properties and functional role of voltage-dependent potassium channels in dendrites of rat cerebellar Purkinje neurons. J Neurosci 23:5698-5707.**

**49.** **Sacco, T., A. De Luca, and F. Tempia. 2006. Properties and expression of Kv3 channels in cerebellar Purkinje cells. Mol Cell Neurosci 33:170-179.**

**50.** **Martina, M., A. E. Metz, and B. P. Bean. 2007. Voltage-dependent potassium currents during fast spikes of rat cerebellar Purkinje neurons: inhibition by BDS-I toxin. J Neurophysiol 97:563-571.**

**51.** **Bushell, T., C. Clarke, A. Mathie, and B. Robertson. 2002. Pharmacological characterization of a non-inactivating outward current observed in mouse cerebellar Purkinje neurones. Br J Pharmacol 135:705-712.**

**52.** **Hodgkin, A. L., and A. F. Huxley. 1952. A quantitative description of membrane current and its application to conduction and excitation in nerve. J Physiol (Lond) 117:500-544.**

**53.** **Huguenard, J. R., and D. A. McCormick. 1992. Simulation of the currents involved in rhythmic oscillations in thalamic relay neurons. J Neurophysiol 68:1373-1383.**

**54.** **Raman, I. M., and B. P. Bean. 1997. Resurgent sodium current and action potential formation in dissociated cerebellar Purkinje neurons. J Neurosci 17:4517-4526.**

**55. Raman, I. M., L. K. Sprunger, M. H. Meisler, and B. P. Bean. 1997. Altered subthreshold sodium currents and disrupted firing patterns in Purkinje neurons of Scn8a mutant mice. Neuron 19:881-891.**

**56. Raman, I. M., and B. P. Bean. 2001. Inactivation and recovery of sodium currents in cerebellar Purkinje neurons: evidence for two mechanisms. Biophys J 80:729-737.**

**57. Edgerton, J. R., and P. H. Reinhart. 2003. Distinct contributions of small and large conductance Ca2+-activated K+ channels to rat Purkinje neuron function. J Physiol (Lond) 548:53-69.**

**58. Womack, M. D., C. Chevez, and K. Khodakhah. 2004. Calcium-activated potassium channels are selectively coupled to P/Q-type calcium channels in cerebellar Purkinje neurons. J Neurosci 24:8818-8822.**

**59. Womack, M. D., and K. Khodakhah. 2002. Characterization of large conductance Ca2+-activated K+ channels in cerebellar Purkinje neurons. Eur J Neurosci 16:1214-1222.**

**60. Cingolani, L. A., M. Gymnopoulos, A. Boccaccio, M. Stocker, and P. Pedarzani. 2002. Developmental regulation of small-conductance Ca2+-activated K+ channel expression and function in rat Purkinje neurons. J Neurosci 22:4456-4467.**

**61. Womack, M. D., and K. Khodakhah. 2003. Somatic and dendritic small-conductance calcium-activated potassium channels regulate the output of cerebellar purkinje neurons. J Neurosci 23:2600-2607.**

**62. Jacquin, T. D., and D. L. Gruol. 1999. Ca2+ regulation of a large conductance K+ channel in cultured rat cerebellar Purkinje neurons. Eur J Neurosci 11:735-739.**

**63. Yazdi, H. H., M. Janahmadi, and G. Behzadi. 2007. The role of small-conductance Ca2+-activated K+ channels in the modulation of 4-aminopyridine-induced burst firing in rat cerebellar Purkinje cells. Brain Res 1156:59-66.**

**64. Xia, X. M., B. Fakler, A. Rivard, G. Wayman, T. Johnson-Pais, J. E. Keen, T. Ishii, B. Hirschberg, C. T. Bond, S. Lutsenko, J. Maylie, and J. P. Adelman. 1998. Mechanism of calcium gating in small-conductance calcium-activated potassium channels. Nature 395:503-507.**

**65. Bond, C. T., J. Maylie, and J. P. Adelman. 1999. Small-conductance calcium-activated potassium channels. Ann N Y Acad Sci 868:370-378.**

**66. Crepel, F., and J. Penit-Soria. 1986. Inward rectification and low threshold calcium conductance in rat cerebellar Purkinje cells. An in vitro study. J Physiol (Lond) 372:1-23.**

**67. Angelo, K., M. London, S. R. Christensen, and M. Hausser. 2007. Local and global effects of I(h) distribution in dendrites of mammalian neurons. J Neurosci 27:8643-8653.**

**68. Khaliq, Z. M., N. W. Gouwens, and I. M. Raman. 2003. The contribution of resurgent sodium current to high-frequency firing in Purkinje neurons: an experimental and modeling study. J Neurosci 23:4899-4912.**

**69. Sacco, T., and F. Tempia. 2002. A-type potassium currents active at subthreshold potentials in mouse cerebellar Purkinje cells. J Physiol (Lond) 543:505-520.**

**70. Harris, K. M., and J. K. Stevens. 1988. Dendritic spines of rat cerebellar Purkinje cells: serial electron microscopy with reference to their biophysical characteristics. J Neurosci 8:4455-4469.**

**71. Napper, R. M., and R. J. Harvey. 1988. Number of parallel fiber synapses on an individual Purkinje cell in the cerebellum of the rat. J Comp Neurol 274:168-177.**

**72. Mittmann, W., U. Koch, and M. Hausser. 2005. Feed-forward inhibition shapes the spike output of cerebellar Purkinje cells. J Physiol 563:369-378.**

**73. Mittmann, W., and M. Hausser. 2007. Linking synaptic plasticity and spike output at excitatory and inhibitory synapses onto cerebellar Purkinje cells. J Neurosci 27:5559-5570.**
**74. Rapp, M., Y. Yarom, and I. Segev. 1992. The impact of parallel fiber background activity on the cable properties of cerebellar Purkinje cells. Neural Comput 4:518-533.**
**75. Albus, J. S. 1971. A theory of cerebellar function. Math Biosci 10:25-61.**
**76. Marr , D. 1969 A theory of cerebellar cortex. J Physiol (Lond) 202:437-470.**
**77. Barbour, B. 1993. Synaptic currents evoked in Purkinje cells by stimulating individual granule cells. Neuron 11:759-769.**
**78. Vincent, P., and A. Marty. 1996. Fluctuations of inhibitory postsynaptic currents in Purkinje cells from rat cerebellar slices. J Physiol (Lond) 494:183-199.**
**79. Llano, I., A. Marty, C. M. Armstrong, and A. Konnerth. 1991. Synaptic- and agonist-induced excitatory currents of Purkinje cells in rat cerebellar slices. J Physiol (Lond) 434:183-213.**
**80. Hsu, Y. H., H. Y. Huang, and M. L. Tsaur. 2003. Contrasting expression of Kv4.3, an A-type K+ channel, in migrating Purkinje cells and other post-migratory cerebellar neurons. Eur J Neurosci 18:601-612.**
**81. Wang, D., and B. G. Schreurs. 2006. Characteristics of IA currents in adult rabbit cerebellar Purkinje cells. Brain Res 1096:85-96.**
**82. Womack, M. D., and K. Khodakhah. 2004. Dendritic control of spontaneous bursting in cerebellar Purkinje cells. J Neurosci 24:3511-3521.**
**83. Womack, M., and K. Khodakhah. 2002. Active contribution of dendrites to the tonic and trimodal patterns of activity in cerebellar Purkinje neurons. J Neurosci 22:10603-10612.**
**84. McKay, B. E., J. D. Engbers, W. H. Mehaffey, G. R. Gordon, M. L. Molineux, J. S. Bains, and R. W. Turner. 2007. Climbing fiber discharge regulates cerebellar functions by controlling the intrinsic characteristics of purkinje cell output. J Neurophysiol 97:2590-2604.**
**85. Rinzel, J. 1975. Spatial stability of traveling wave solutions of a nerve conduction equation. Biophys J 15:975-988.**
**86. Grinford, P. 1991. Patterns and Waves: The Theory and Application of Reaction-diffusion Equations. Clarendon, Oxford.**
**87. Champneys, A. R., Y. A. Kuznetsov, and B. Sandstede. 1996. A numerical toolbox for homoclinic bifurcation analysis. Int J Bifurc Chaos 6:867-887.**
**88. Cranck, J. 1956. The Mathematics of Diffusion. Clarendon, Oxford.**
**89. Press, W. H., S. A. Teukolsky, W. T. Vetterling, and B. P. Flannery. 1994. Nurmerical Recipes in C. Cambridge UP, Cambridge.**
**90. Segev, I., and W. Rall. 1998. Excitable dendrites and spines: earlier theoretical insights elucidate recent direct observations. Trends Neurosci 21:453-460.**
**91. Stockbridge, N. 1988. Theoretical response to trains of action potentials of a bifurcating axon with one short daughter branch. Biophys J 54:637-641.**
**92. Segev, I., and M. London. 2000. Untangling dendrites with quantitative models. Science 290:744-750.**
**93. Rall, W. 1959. Branching dendritic trees and motoneuron membrane resistivity. Exp Neurol 1:491-527.**
**94. Rapp, M., I. Segev, and Y. Yarom. 1994. Physiology, morphology and detailed passive models of guinea-pig cerebellar Purkinje cells. J Physiol (Lond) 474:101-118.**

**95. Segev, I., M. Rapp, Y. Manor, and Y. Yarom. 1992. Analog and ditial processing in nerve cells: dendritic integration and axonal propagation. In Single Neuron Computation. T. McKenna, J. Davis J and S.F. Zornetzer, editors. Academic Press, Boston. 173-198.**

**96. Li, Y. X., R. Bertram, and J. Rinzel. 1996. Modeling N-methyl-D-aspartate-induced bursting in dopamine neurons. Neuroscience 71:397-410.**

**97. Jack, J. J. B., D. Noble, and R. W. Tsien. 1983. Electric Current Flow in Excitable Cells. Oxford University Press, Oxford.**